

Study of extragalactic H II regions with échelle spectroscopy: The A2 region in the irregular galaxy IC 4662

Alexei Y. Kniazev^{1,2,3}

¹ South African Astronomical Observatory, Cape Town, 7935, South Africa a.kniazev@sao.nrf.ac.za

² Southern African Large Telescope, Cape Town, 7935, South Africa

³ Sternberg State Astronomical Institute, Moscow, Universitetsky ave., 13, Russia

Received 2025 January 02; accepted 20xx month day

Abstract I present the results of échelle spectroscopy of a bright H II region in the irregular galaxy IC 4662 and their comparison with results from long-slit spectroscopy of the same region. All observations were obtained with the standard spectrographs of the SALT telescope: (1) low and medium spectral resolution spectrograph RSS ($R \approx 800$) and (2) échelle spectrograph HRS ($R = 16000-17000$). In both types of data the intensities of most of the emission lines were measured and abundances of oxygen and N, Ne, S, Ar, Cl and Fe were determined as well as physical parameters of the H II region. The chemical abundances were obtained from both types of data with the T_e -method. Abundances calculated from both types of data agree to within the cited uncertainties. The analysis of the échelle data revealed three distinct kinematic subsystems within the studied H II region: a narrow component (NC, $\sigma \approx 12$ km/s), a broad component (BC, $\sigma \approx 40$ km/s), and a very broad component (VBC, $\sigma \approx 60 - 110$ km/s, detected only in the brightest emission lines). The elemental abundances for the NC and BC subsystems were determined using the T_e -method. The velocity dispersion dependence on the ionisation potential of elements showed no correlation for the NC, indicating a well-mixed turbulent medium, while the BC exhibited pronounced stratification, characteristic of an expanding shell. Based on a detailed analysis of the kinematics and chemical composition, it was concluded that the BC is associated with the region surrounding a Wolf-Rayet star of spectral type WN7-8. The stellar wind from this WR star interacts with a shell ejected during an earlier evolutionary stage (either as a red supergiant or a luminous blue variable, LBV), which is enriched in nitrogen. These findings highlight the importance of high spectral resolution for detecting small-scale (~ 25 pc) chemical inhomogeneities and for understanding the feedback mechanisms of massive stars in low-metallicity environments.

Key words: galaxies: abundances — galaxies: irregular — galaxies: evolution — galaxies: individual (IC 4662)

1 INTRODUCTION

The study of extragalactic H II regions by spectroscopy usually involves several fairly standard methods: (1) long slit spectroscopy; (2) multi-object spectroscopy; (3) panoramic spectroscopy; (4) Fabry-Perot spectroscopy; (5) échelle spectroscopy. Each of these methods has advantages and disadvantages, and each has a specific area of application. Only panoramic and échelle spectroscopy methods can be used for the high-resolution ($R > 10000$) spectrophotometry of extragalactic H II regions in a large spectral range. In the case of panoramic spectroscopy it is usually necessary to use several spectral configurations to

cover a large spectral range, which requires stable weather conditions. This usually results in a spectral resolution of $R < 5000$ (Izotov et al. 2006a; James et al. 2009, 2013b,a). Two problems, limited slit length for sky spectrum subtraction and blaze correction, appear when échelle spectroscopy is used. However, both these problems can be reasonably well resolved by using a fibre échelle spectrograph.

This paper presents the possibility of the study of chemical abundances in bright extragalactic H II regions using the high-resolution échelle spectrograph at the Southern African Large Telescope (SALT; Buckley et al. 2006; O’Donoghue et al. 2006). Such a possibility will be

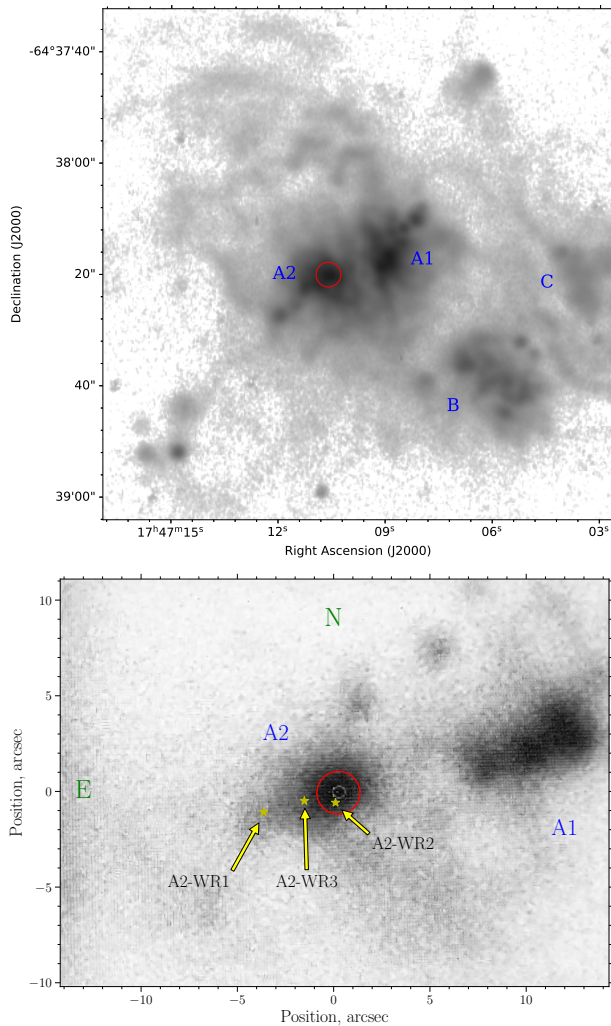


Fig. 1 **Left panel:** The central part of the $H\alpha$ IC 4662 galaxy image. The image was taken with the ESO 2.2m telescope (Kaisin et al. 2007). The image is displayed on a logarithmic scale to show the bright and faint $H\alpha$ regions at the same time. Darker objects indicate brighter sources of $H\alpha$ emission. The red circle shows the position of the HRS fibre ($2.23''$ in diameter) during the échelle observations. The spectral slit during observations with the RSS spectrograph also passed through the same region. **Right panel:** The image from the HRS guiding system with size of 28.5×21.3 arcsecs. The HRS guiding system has no filter and its maximum sensitivity is at $\sim 6000 \text{ \AA}$. The red circle is the exact position of the HRS fibre (diameter $2.23''$) during the échelle observations. Yellow stars and arrows show positions and names of WR stars found by Crowther & Bibby (2009). At the assumed galaxy distance of 2.44 Mpc (Kaisin et al. 2007), $1'' = 11.8 \text{ pc}$. The naming system for H II regions is taken from Heydari-Malayeri et al. (1990).

demonstrated by comparison of chemical abundances in a bright H II region of the IC 4662 galaxy, obtained by two spectroscopic methods – long-slit and échelle.

IC 4662 is a gas rich, metal poor, dwarf irregular galaxy at a distance of about 2.5 Mpc. It does not belong to any group and has no massive neighbors. However, the galaxy is actively star-forming and several giant H II regions are visible. The radio and infrared data show that very strong star formation is going on in the brightest H II regions which is still weakly visible in the optical (Johnson et al. 2003; Gilbert & Vacca 2009). The galaxy contains Wolf-Rayet (WR) stars (Crowther & Bibby 2009), and its star formation history has been investigated by McQuinn et al. (2009, 2010a,b). van Eymeren et al. (2010) has examined in detail the H I in IC 4662 and has detected a giant cloud of H I around this galaxy. The first detailed analysis of the chemical abundance of the H II regions of this galaxy was done by Heydari-Malayeri et al. (1990), where it was shown that the two brightest H II regions have very similar chemical abundances. In Hidalgo-Gómez et al. (2001) it was shown that there is a fainter H II region on the edge of IC 4662, which has a metallicity significantly different (0.5 dex) from the metallicities of the central H II region.

This article is organised as follows: Section 2 describes observations and data reduction. Section 3 briefly describes the methodology of the analysis. Section 4 presents results of our analysis, and their discussion is presented in Section 5.

2 SPECTRAL OBSERVATIONS AND DATA REDUCTION

2.1 Long-slit observations

The long-slit spectral observations of the H II region A2 in the IC 4662 galaxy (see Figure 1) were carried out during SALT commissioning on April 25th, 2006 with the Robert Stobie Spectrograph, (RSS hereafter; Burgh et al. 2003; Kobulnicky et al. 2003) which is a spectrograph of low and medium spectral resolution. Observations were done with an image quality of $1''.4$. A mosaic of three CCDs is used as the detector on the RSS, with the total mosaic size being 6144×4096 pixels. The pixel size along the slit is $0''.129$ and the total slit length is $8'$. A binning factor of 2 was used during observations of IC 4662 resulting in a pixel size along the slit of $0''.258$. The observations were carried out with a spectral configuration covering the spectral range $3650\text{--}6750 \text{ \AA}$. The Volume Phase Holographic (VPH) grating, PG900, was used with a final reciprocal dispersion of about 0.97 \AA per pixel. A slit width of $1''.5$ resulted in a spectral resolution of $R \sim 800$ ($\text{FWHM} \sim 4.8 \text{ \AA}$). Two 600 sec exposures were made, followed by a reference spectrum of a CuAr lamp and spec-

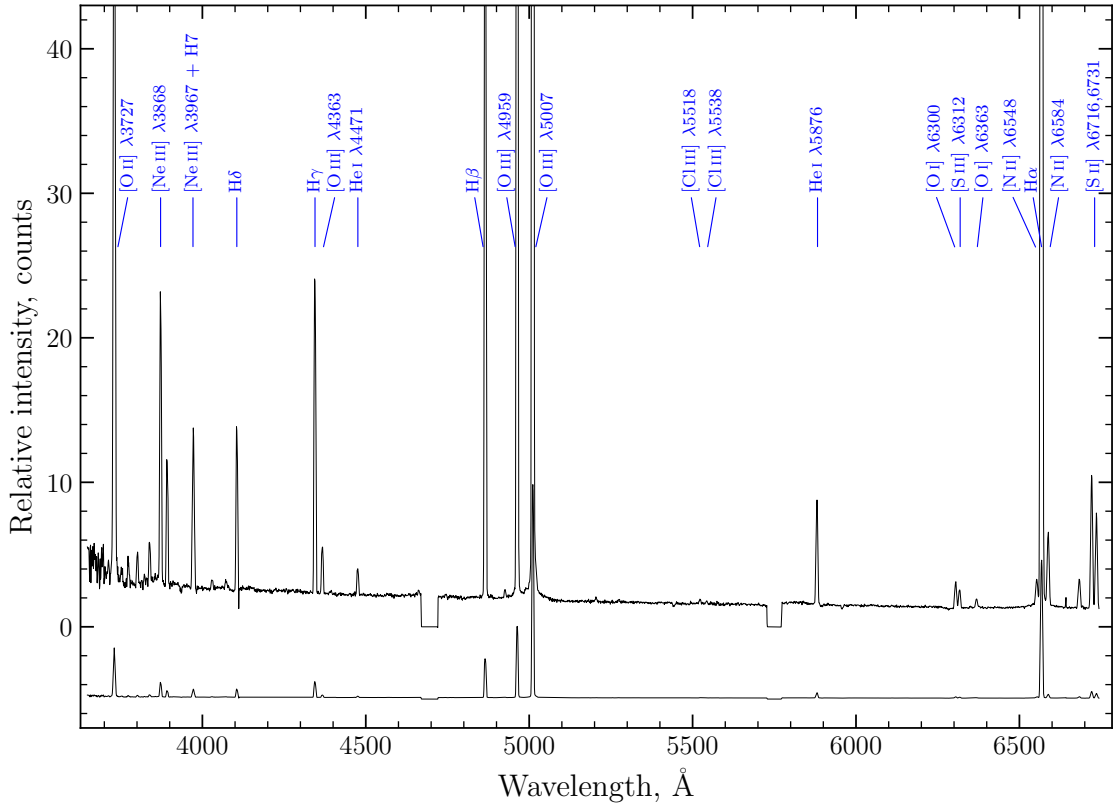


Fig. 2 One dimensional spectrum of the A2 region obtained with a long slit in the spectral region 3650–6750 Å. All major emission lines are shown and their measurements are given in Table 3. The spectrum at the bottom is scaled and shifted to show the relative intensities of strong lines. Two gaps between the CCDs in the mosaic are obvious, with no data there.

tral flat-fields. Zero level (bias) images were also taken for a standard processing of the two-dimensional spectra. In order to get the correct relative energy distribution, spectra of the spectrophotometric standard EG 21 (Hamuy et al. 1992, 1994) were obtained during astronomical twilight. SALT is a telescope with a variable pupil, so that the illuminating beam changes continuously during the observations. This makes absolute flux calibration impossible even when using spectrophotometric standards. However, the relative energy distributions are very accurate, especially as the SALT has an atmospheric dispersion compensator (ADC).

The primary data reduction was done using the standard SALT pipeline (Crawford et al. 2010), and the following preliminary and spectral data reduction were done using an RSS spectral pipeline Kniazev (2021). For the analysis presented in this paper, a one-dimensional spectrum of the A2 region (9 pixels or $2''3$) was extracted from the two-dimensional reduced spectrum. This spectrum is shown in Figure 2, where the most important emission lines are labelled.

2.2 Échelle observations

Spectral observations of the A2 region of the galaxy IC 4662 employing the High Resolution Fibre échelle Spectrograph (HRS; Barnes et al. 2008; Bramall et al. 2010, 2012; Crause et al. 2014) were carried out on 11 October 2017. A single exposure of 2400 sec duration was performed with seeing of $1''.5$. The HRS is a thermostabilised double-beam échelle spectrograph, with the entire optical part housed in a vacuum to reduce temperature and mechanical influences. The blue arm of the spectrograph covers the spectral range of 3735–5580 Å, and the red arm covers the spectral range of 5415–8870 Å, respectively. The spectrograph can be used in low (LR, $R \approx 14,000$ –15,000) medium (MR, $R \approx 40,000$ –43,000) and high (HR, $R \approx 67,000$ –74,000) resolution modes and is equipped with two fibres (object and sky fibres) for each mode. During observations of the A2 region the LR mode was used with fibres of $2''.23$ diameter. Both CCD detectors, for the blue and red arms, were read out with a binning of 1×1 .

All standard calibrations for HRS are done once a week, which is technically sufficient to achieve a spectral accuracy of 400 – 500 m s^{-1} for the LR mode. The current HRS calibration plan includes: (1) three flat-field spectra

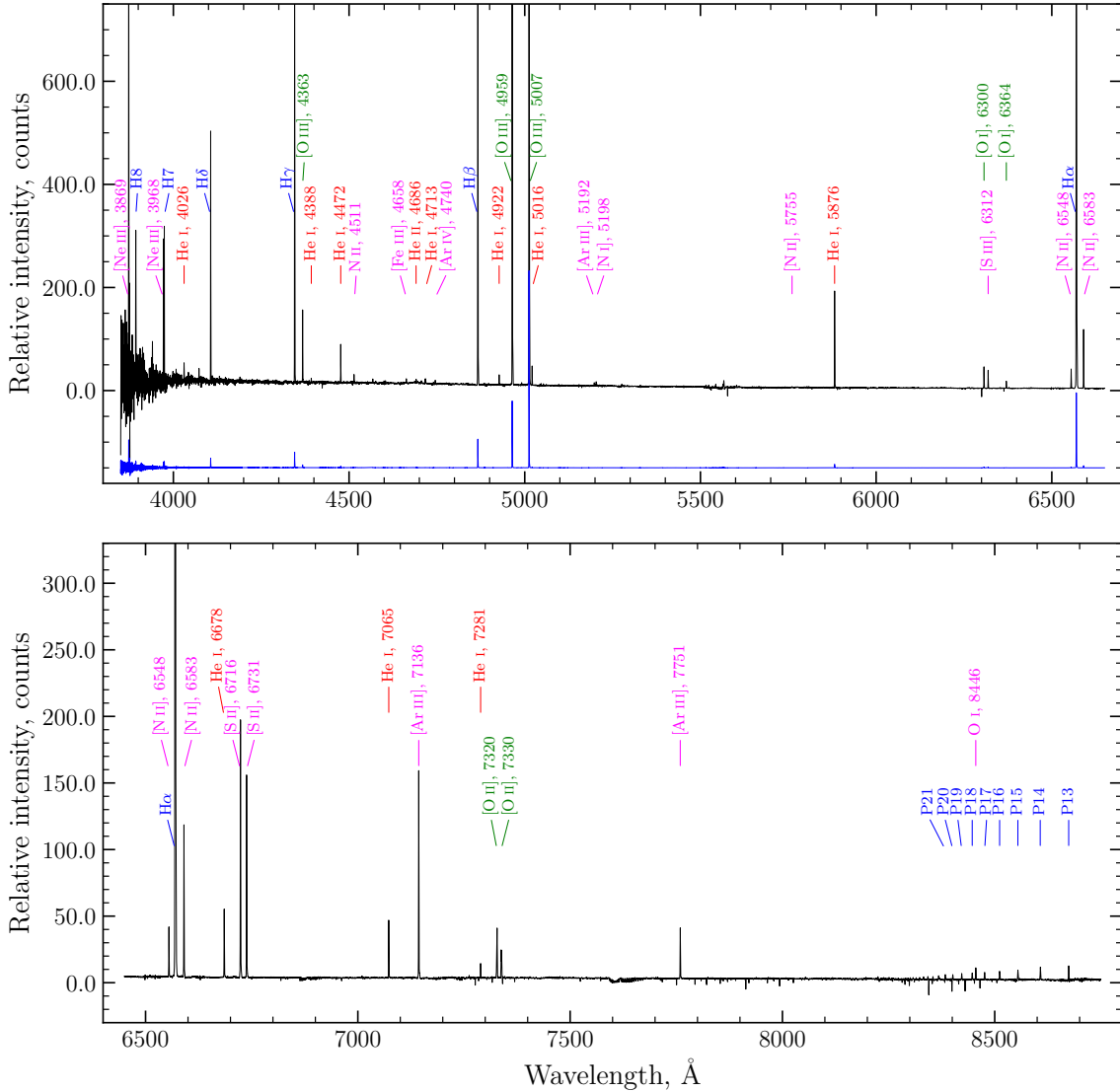


Fig. 3 The final échelle spectrum of the A2 region shown in two panels (74 spectral orders were merged, and corrected for the sensitivity curve). All the main emission lines are shown and their intensities are presented in Table 3. In the upper panel, the spectrum is again displayed, compressed vertically by a factor of 20 and shifted downwards to show the relative strengths of the strongest lines.

to find the positions of all spectral échelle orders and correct for the effect of the brightness distribution along each échelle order (blaze correction) and (2) one (Th+Ar) lamp spectrum for wavelength calibration. Also, 11 bias images are taken at the beginning of each observational night for subsequent zero-offset accounting. Once a week, one velocity standard is observed in all modes to check the accuracy of the wavelength calibration. All velocity standards have a velocity accuracy better than 20 m s^{-1} (see for details Kniazev et al. 2019). An HRS spectrophotometric standard is observed once per month. All HRS spectrophotometric standards have spectral distributions known in steps of 3–4 Å.

The primary HRS data reduction was performed automatically using the SALT standard pipeline (Crawford et al. 2010) and the following échelle data reduction was done using the HRS pipeline described in detail in Kniazev et al. (2016, 2019). It should be noted here that the algorithm for constructing a two-dimensional dispersion curve is the same for all HRS modes, but the optical path of the light in each mode is slightly different and the wavelength calibration result is different for different modes. Initial and final wavelengths for each échelle order in the LR mode, the number of identified lines used and the final solution accuracy for each order are given in Tables 1 and 2. An improved version of the pipeline has been used

for HRS data since September 2020: (1) the removal of scattered light between orders has been significantly improved, and (2) stability of the wavelength extraction and calibration for the five bluer échelle orders up to wavelength $\approx 3732 \text{ \AA}$ has been improved. Thus, 41 échelle orders are now extracted and calibrated in the blue region.

FWHM measured over all lines found in the reduced reference spectra varies from $\approx 0.25 \text{ \AA}$ to $\approx 0.34 \text{ \AA}$ for the blue arm spectrum and from $\approx 0.33 \text{ \AA}$ to $\approx 0.53 \text{ \AA}$ for the red arm spectrum. The change in the half-width of the instrumental profile as a function of wavelength is shown in Figure 4. The behaviour of the instrumental profile is well approximated by a first order polynomial and can be written in the form:

$$\text{FWHM}(\lambda) = 6.4148 \cdot 10^{-5} \cdot \lambda - 9.1383 \cdot 10^{-3}, \quad (1)$$

for the blue spectrum in the spectral region 3715–5580 \AA giving an accuracy of 0.007 \AA , and

$$\text{FWHM}(\lambda) = 5.9818 \cdot 10^{-5} \cdot \lambda + 4.9624 \cdot 10^{-3}, \quad (2)$$

for the red spectrum in the spectral region 5415–8870 \AA giving an accuracy of 0.006 \AA .

The spectral resolution $R = \lambda/\delta\lambda$ as a function of wavelength is shown in Figure 5. As can be seen from the figure, the resulting resolution range, $R=16,000\text{--}16,600$, is slightly higher than published for the spectrograph, viz., $R=14,000\text{--}15,000$ ¹, but the difference is no more than 10%. The final échelle spectrum of the A2 region, comprising 74 spectral orders merged and corrected for the sensitivity curve, is shown in Figure 3. The most important emission lines visible on this spectrum are indicated.

3 PHYSICAL CONDITIONS AND DETERMINATION OF HEAVY-ELEMENT ABUNDANCES

All emission lines for both types of data have been measured using programs described in detail in Kniazev et al. (2004). The programs can measure the emission line intensities in two ways: (1) as the total flux exceeding a fitted continuum at some wavelength interval and then the shape of the lines is not taken into account, or (2) by fitting a Gaussian function (or number of Gaussians) to the observed flux distribution exceeding the fitted continuum in some wavelength interval. Usually, method (1) is used except for situations when two measured lines are close to each other and their fluxes overlap and it is necessary to separate them. It is important to estimate the total measurement errors of the line fluxes as a combination of the errors: (1) errors of continuum fitting, (2) errors due to the

¹ http://pysalt.salt.ac.za/proposal_calls/current/ProposalCall.html

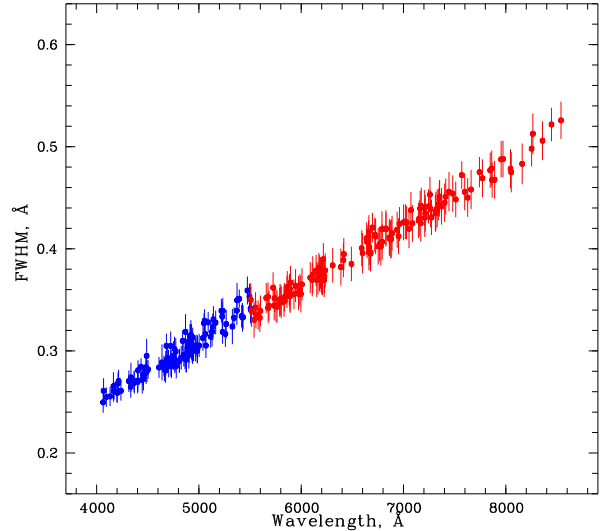


Fig. 4 Wavelength dependence of FWHM for the blue and red arms for the LR mode.

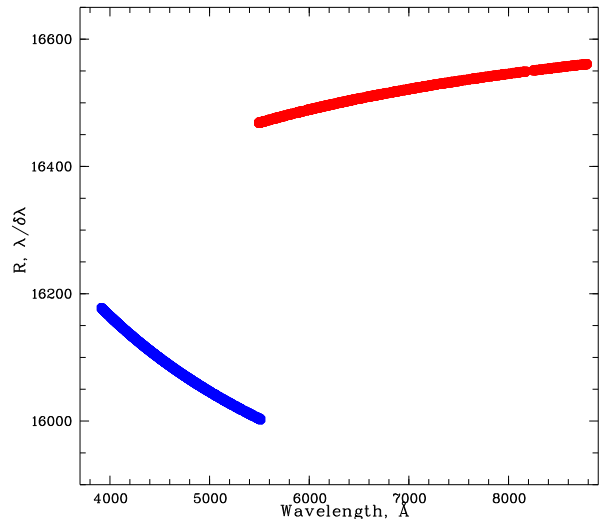


Fig. 5 Spectral resolution, $R = \lambda/\delta\lambda$, as a function of wavelength for the blue and red arms, for the LR mode.

Poisson statistics of photons in lines, and (3) errors of the spectral sensitivity curve. For the described observations the error (3) was about 2% for both types of data. All error components were summed quadratically and the total error in the line intensities was used by the programs to calculate the error of the output physical parameters and chemical composition. It should be noted here that the original set of programs described in Kniazev et al. (2004) was created in the standard astronomical data processing system, MIDAS, which, since April 2012, is no longer officially supported by the European Southern Observatory (ESO). For this reason the author has rewritten all the relevant MIDAS programs in Python.

Table 1 Spectral orders for the HRS blue arm in LR mode

#	Spectral Order	Spectral Lines	Object Fiber		RMS (Å)	Spectral Lines	Sky Fiber		RMS (Å)
			λ_0 (Å)	λ_{end} (Å)			λ_0 (Å)	λ_{end} (Å)	
1	124	1	3732.48	3782.27	0.05051	1	3732.49	3782.26	0.04968
2	123	1	3762.92	3812.99	0.15497	1	3762.92	3812.98	0.15412
3	122	5	3792.01	3844.50	0.01361	5	3792.01	3844.50	0.01361
4	121	3	3825.28	3875.94	0.08576	3	3825.28	3875.94	0.08487
5	120	5	3857.32	3908.02	0.00446	4	3857.20	3908.31	0.01274
6	119	8	3889.94	3940.96	0.00755	7	3889.88	3941.04	0.00703
7	118	8	3922.74	3974.40	0.00443	12	3923.06	3974.35	0.01131
8	117	9	3956.49	4008.26	0.00674	8	3956.91	4008.34	0.00581
9	116	9	3990.43	4042.80	0.00858	10	3990.75	4042.91	0.00777
10	115	15	4025.33	4077.92	0.00481	15	4025.42	4078.04	0.00824
11	114	16	4060.75	4113.65	0.00337	17	4060.78	4113.77	0.00749
12	113	13	4096.71	4149.99	0.00607	12	4096.82	4150.10	0.00392
13	112	8	4133.33	4186.99	0.00519	10	4133.42	4187.10	0.00705
14	111	15	4170.67	4224.69	0.00474	16	4170.79	4224.79	0.00664
15	110	15	4208.60	4263.07	0.00530	16	4208.72	4263.19	0.00449
16	109	19	4247.25	4302.13	0.00722	17	4247.37	4302.24	0.00750
17	108	11	4286.49	4342.04	0.01378	11	4286.57	4342.18	0.00920
18	107	13	4326.76	4382.45	0.00591	16	4326.87	4382.57	0.00704
19	106	16	4367.61	4423.76	0.00873	14	4367.73	4423.89	0.00397
20	105	16	4409.27	4465.84	0.00677	14	4409.41	4465.94	0.00694
21	104	13	4451.66	4508.74	0.00692	14	4451.79	4508.86	0.00752
22	103	19	4494.93	4552.51	0.00939	17	4495.07	4552.60	0.00584
23	102	17	4539.06	4597.08	0.00800	15	4539.16	4597.22	0.00960
24	101	17	4584.05	4642.54	0.00881	15	4584.15	4642.74	0.00763
25	100	19	4629.93	4688.96	0.00775	18	4630.06	4689.08	0.00783
26	99	18	4676.75	4736.16	0.00843	16	4676.84	4736.44	0.00682
27	98	14	4724.46	4784.57	0.00842	12	4724.58	4784.70	0.00724
28	97	17	4773.15	4833.88	0.00987	17	4773.33	4834.00	0.00858
29	96	19	4822.94	4884.21	0.00677	19	4823.06	4884.34	0.00615
30	95	19	4873.73	4935.60	0.00854	20	4873.86	4935.73	0.00888
31	94	15	4925.58	4988.09	0.00907	15	4925.75	4988.21	0.00750
32	93	8	4978.59	5041.46	0.00803	8	4978.72	5041.47	0.00999
33	92	13	5032.68	5096.55	0.00598	7	5031.72	5096.63	0.00518
34	91	15	5088.03	5152.46	0.00802	14	5088.16	5152.61	0.00687
35	90	17	5144.58	5209.67	0.00677	15	5144.68	5209.84	0.00741
36	89	16	5202.33	5268.20	0.00882	15	5202.45	5268.36	0.00836
37	88	17	5261.44	5328.06	0.00714	15	5261.53	5328.22	0.00629
38	87	15	5321.89	5389.38	0.01154	12	5322.05	5389.52	0.00982
39	86	16	5383.82	5451.94	0.01082	15	5383.97	5452.09	0.00978
40	85	16	5447.09	5516.12	0.00785	15	5447.24	5516.27	0.00640
41	84	6	5511.89	5581.96	0.00486	7	5512.05	5582.06	0.00190

The analysis of the emission spectra was carried out within the classical two-zone model of the H II region. This methodology is described in detail in Kniazev et al. (2004, 2005, 2008); Kniazev (2012). The chemical element contents of O, N, Ne, S, Ar, Cl and Fe as well as physical parameters such as the electron temperature (T_e) and electron density (N_e) were determined using this methodology. All the above parameters and their errors were determined taking into account the errors of the emission line intensities measured in the previous step. The spectral data for the A2 region in IC 4662 covered the whole required spectral range in both cases, although in the case of the long-slit spectra the lines of He II $\lambda 4686$ Å and [N II] $\lambda 5755$ Å were lost due to the gaps between the CCDs in the RSS mosaic. For this reason two independent electron temperatures were used in the calculations based on the échelle data: $T_e(\text{O III})$ for the hot zone and $T_e(\text{N II})$ for the cold zone. The former was calculated from the line ratios of

[O III] $\lambda\lambda 4363, 4959, 5007$ Å, and the second from the line ratios of [N II] $\lambda\lambda 5755, 6548, 6584$ Å. The total oxygen abundance was calculated as:

$$\frac{O}{H} = \frac{O^+}{H} + \frac{O^{++}}{H} + \frac{O^{+++}}{H} \quad (3)$$

In the case of the long-slit data, the cold zone temperature was calculated from an approximation based on the hot zone temperature using equations from Izotov et al. (2006b), and the total oxygen abundance was calculated without O^{+++}/H , as this requires the presence of the He II $\lambda 4686$ Å line. However, it should be noted here that the measured intensity of this line in the échelle data is less than 1% of the intensity of the $H\beta$ line and, therefore, the contribution of O^{+++}/H is very small and does not exceed the accuracy of the total abundance of oxygen (Tables 3 and 4).

Table 2 Spectral orders for the HRS red arm in LR mode

#	Spectral Order	Spectral Lines	Object Fiber		RMS (Å)	Spectral Lines	Sky Fiber		RMS (Å)
			λ_0 (Å)	λ_{end} (Å)			λ_0 (Å)	λ_{end} (Å)	
1	85	4	5413.92	5531.27	0.00378	5	5413.71	5531.16	0.00383
2	84	11	5478.41	5597.11	0.00510	9	5478.21	5596.98	0.00621
3	83	7	5544.45	5664.53	0.00238	10	5544.26	5664.39	0.00400
4	82	13	5612.10	5733.59	0.00388	14	5611.91	5733.44	0.00522
5	81	12	5681.42	5804.36	0.00450	12	5681.24	5804.19	0.00590
6	80	10	5752.48	5876.89	0.00246	9	5752.30	5876.72	0.00358
7	79	12	5825.33	5951.26	0.00265	15	5825.16	5951.08	0.00395
8	78	15	5900.05	6027.54	0.00465	16	5899.88	6027.34	0.00430
9	77	21	5976.71	6105.79	0.00449	22	5976.54	6105.59	0.00518
10	76	18	6055.39	6186.11	0.00728	21	6055.22	6185.90	0.00575
11	75	19	6136.17	6268.56	0.00509	24	6136.00	6268.35	0.00539
12	74	17	6219.13	6353.24	0.00525	21	6218.96	6353.03	0.00659
13	73	14	6304.36	6440.24	0.00341	16	6304.19	6440.02	0.00527
14	72	9	6391.96	6529.66	0.00414	17	6391.78	6529.44	0.00382
15	71	13	6482.02	6621.60	0.00844	13	6481.85	6621.37	0.00803
16	70	17	6574.66	6716.16	0.00534	23	6574.48	6715.93	0.00613
17	69	13	6669.98	6813.46	0.00640	15	6669.80	6813.23	0.00559
18	68	11	6768.10	6913.63	0.00463	15	6767.92	6913.40	0.00427
19	67	14	6869.15	7016.78	0.00600	16	6868.96	7016.55	0.00625
20	66	13	6973.26	7123.06	0.00483	17	6973.07	7122.84	0.00502
21	65	16	7080.57	7232.62	0.00498	18	7080.38	7232.39	0.00553
22	64	18	7191.24	7345.59	0.00437	18	7191.04	7345.36	0.00626
23	63	17	7305.42	7462.16	0.00552	17	7305.21	7461.93	0.00514
24	62	11	7423.27	7582.48	0.00518	12	7423.06	7582.25	0.00672
25	61	14	7544.99	7706.75	0.00548	13	7544.77	7706.52	0.00495
26	60	7	7670.77	7835.16	0.00420	7	7670.54	7834.94	0.00458
27	59	13	7800.80	7967.93	0.00695	13	7800.57	7967.70	0.00583
28	58	13	7935.32	8105.28	0.00803	12	7935.09	8105.05	0.00763
29	57	7	8074.56	8247.45	0.00764	5	8074.32	8247.22	0.00753
30	56	6	8218.76	8394.70	0.00537	6	8218.52	8394.46	0.00569
31	55	7	8368.21	8547.31	0.00679	8	8367.96	8547.06	0.00356
32	54	8	8523.18	8705.57	0.00598	7	8522.93	8705.32	0.00681
33	53	7	8684.01	8869.81	0.00418	3	8683.75	8869.54	0.00216

4 RESULTS

Intensities of measured emission lines $F(\lambda)$ reduced to intensities of the $H\beta$ line, and the same intensities $I(\lambda)$ corrected for interstellar absorption and underlying Balmer absorption are presented in Table 3 for both spectra, together with the equivalent width $EW(H\beta)$ of the $H\beta$ emission line, the equivalent width $EW(abs)$ of the Balmer absorption lines, the extinction coefficient $C(H\beta)$ and the extinction $E(B-V)$ value calculated from it. The obtained extinction is the total extinction on the line-of-sight, being the sum of (1) the intrinsic extinction in the IC 4662 galaxy, (2) the intergalactic extinction, and (3) the foreground extinction in our Galaxy. The derived electron temperatures T_e and electron densities N_e , and the calculated abundances of oxygen, nitrogen, neon, sulphur, argon, chlorine and iron are given in columns (2)–(4) of Table 4.

4.1 Physical parameters and abundances of chemical elements in the long-slit and échelle observations

The line intensities presented in Table 3 show that two quite close but not exactly overlapping parts of the H II region A2 were apparently observed. This is obvious since

in the case of the long-slit observation, a slit $1''.5$ wide was used, while in the case of the échelle observations a circular fibre of $2''.23$ in diameter was used. The image quality in both observations was very close to $1''.4$ and $1''.5$ respectively. Nevertheless, it should be noted that the intensities of most of the lines correlate quite well with each other. Exactly the same conclusion can be drawn regarding the measured equivalent width of the emission line $H\beta$ and the estimated equivalent width of the Balmer absorption lines $EW(abs)$, which are in good agreement with each other taking into account their errors. This agreement can be seen in the calculated temperatures, densities and chemical element abundances given in columns (2)–(4) of Table 4. The electron densities calculated from the sulphur lines, $[S II] \lambda\lambda 6717, 6731 \text{ \AA}$, differ most strongly and the main reason seems to be that the line $[S II] \lambda 6731 \text{ \AA}$ is at the very edge of the long-slit spectrum (Figure 2). This could introduce an additional systematic error into its flux measurement. However, the measured electron densities are so small in absolute value (and this is normal in H II regions) that even a difference of a factor of two does not result in a large difference in calculated abundances between the two spectra. As already mentioned in Section 3 in the case

Table 3 Emission line intensities in the A2 region measured with different types of observation

$\lambda_0(\text{\AA})$ Ion	Long-slit		Échelle (total flux)	
	$F(\lambda)/F(H\beta)$	$I(\lambda)/I(H\beta)$	$F(\lambda)/F(H\beta)$	$I(\lambda)/I(H\beta)$
3727 [O II]	1.276±0.028	1.720±0.041	–	–
3869 [Ne III]	0.368±0.009	0.475±0.012	0.5763±0.0453	0.6776±0.0536
3889 H 8	–	–	0.1877±0.0194	0.2198±0.0229
3889 He I + H8	0.149±0.005	0.218±0.008	–	–
4026 He I	0.009±0.002	0.011±0.002	0.0146±0.0019	0.0167±0.0022
4069 [S II]	–	–	0.0106±0.0016	0.0120±0.0019
4101 H δ	0.193±0.005	0.255±0.007	0.2731±0.0035	0.3121±0.0053
4340 H γ	0.398±0.009	0.467±0.011	0.4843±0.0144	0.5277±0.0160
4363 [O III]	0.060±0.003	0.067±0.004	0.0693±0.0010	0.0747±0.0011
4471 He I	0.031±0.002	0.034±0.002	0.0387±0.0017	0.0410±0.0018
4658 [Fe III]	–	–	0.0046±0.0004	0.0047±0.0004
4686 He II	–	–	0.0082±0.0008	0.0084±0.0009
4713 He I	–	–	0.0055±0.0004	0.0056±0.0004
4740 [Ar IV]	0.005±0.002	0.005±0.002	0.0036±0.0004	0.0036±0.0004
4861 H β	1.000±0.010	1.000±0.011	1.0000±0.0022	1.0000±0.0031
4922 He I	0.015±0.002	0.014±0.002	0.0104±0.0006	0.0103±0.0006
4959 [O III]	1.847±0.042	1.780±0.041	1.8829±0.0042	1.8515±0.0041
5007 [O III]	5.588±0.125	5.327±0.121	5.6433±0.1419	5.5112±0.1395
5016 He I	–	–	0.0204±0.0009	0.0199±0.0009
5192 [Ar III]	–	–	0.0021±0.0002	0.0020±0.0002
5199 [N I]	–	–	0.0043±0.0003	0.0041±0.0003
5200 [N I]	–	–	0.0012±0.0003	0.0011±0.0002
5518 [Cl III]	0.004±0.001	0.004±0.001	0.0068±0.0009	0.0062±0.0008
5538 [Cl III]	0.003±0.001	0.002±0.001	0.0032±0.0005	0.0029±0.0004
5755 [N II]	–	–	0.0015±0.0002	0.0013±0.0002
5876 He I	0.145±0.004	0.115±0.003	0.1301±0.0012	0.1136±0.0010
6300 [O I]	0.034±0.002	0.025±0.001	0.0299±0.0009	0.0249±0.0008
6312 [S III]	0.023±0.001	0.017±0.001	0.0232±0.0004	0.0193±0.0003
6364 [O I]	0.012±0.001	0.009±0.001	0.0096±0.0005	0.0079±0.0004
6548 [N II]	0.039±0.001	0.028±0.001	0.0266±0.0004	0.0216±0.0003
6563 H α	4.020±0.088	2.840±0.069	3.4883±0.0067	2.8310±0.0060
6583 [N II]	0.118±0.006	0.083±0.004	0.0814±0.0008	0.0659±0.0006
6678 He I	0.043±0.002	0.030±0.001	0.0372±0.0011	0.0299±0.0009
6716 [S II]	0.186±0.004	0.128±0.003	0.1500±0.0007	0.1199±0.0005
6731 [S II]	0.137±0.003	0.094±0.003	0.1146±0.0005	0.0915±0.0004
7065 He I	–	–	0.0334±0.0011	0.0259±0.0008
7136 [Ar III]	–	–	0.1129±0.0009	0.0869±0.0007
7281 He I	–	–	0.0077±0.0004	0.0059±0.0003
7320 [O II]	–	–	0.0341±0.0010	0.0258±0.0008
7330 [O II]	–	–	0.0285±0.0007	0.0216±0.0006
7751 [Ar III]	–	–	0.0284±0.0009	0.0208±0.0007
8374 P 21	–	–	0.0027±0.0003	0.0019±0.0002
8392 P 20	–	–	0.0038±0.0003	0.0026±0.0002
8413 P 19	–	–	0.0044±0.0003	0.0031±0.0002
8438 P 18	–	–	0.0048±0.0003	0.0034±0.0002
8467 P 17	–	–	0.0052±0.0003	0.0036±0.0002
8502 P 16	–	–	0.0065±0.0004	0.0045±0.0002
8545 P 15	–	–	0.0077±0.0005	0.0053±0.0003
8598 P 14	–	–	0.0097±0.0004	0.0067±0.0003
8665 P 13	–	–	0.0110±0.0006	0.0076±0.0004
EW(abs) Å	2.40±0.25		2.00±0.24	
EW(H β) Å	137±6		114±4	
C(H β) dex	0.36±0.050		0.27±0.01	
E(B-V) mag	0.25±0.040		0.18±0.01	

of the échelle spectrum, the abundance of O^{+++} was also taken into account for the calculation of the total abundance of oxygen. This was calculated using the intensity of the He II $\lambda 4686$ Å line [Kniazev et al. \(2008\)](#). However, as can be seen in Table 4, the abundance of this ion is less than 0.5% and therefore its contribution is negligibly small.

Overall, with an exposure difference of a factor of two, the échelle spectrum allows measurement of emission lines

at 0.12–0.15% of H β intensity with a signal-to-noise ratio about four, while in the long-slit spectrum the weakest lines are lines at 0.3% of the H β intensity with a signal-to-noise ratio about three. Of course, this is due to the difference in spectral resolution and it is quite obvious that this advantage of échelle spectroscopy will disappear quickly towards fainter objects.

Table 4 Physical conditions and chemical element abundances in the A2 region for different types of observation and in the different kinematic subsystems found with the échelle data

Value (1)	Long-slit (2)	Échelle (total flux)		Échelle (subsystems)	
		$T_e(\text{OII})$ (3)	$T_e(\text{NII})$ (4)	Narrow (5)	Wide (6)
$T_e(\text{OIII})(\text{K})$	12,551±278	12,929±121	12,929±121	13,194±248	12,169±494
$T_e(\text{OII})(\text{K})$	12,295±224	12,591±92	12,591±92	12,788±180	13,160±380
$T_e(\text{NII})(\text{K})$	–	11,790±924	11,790±924	–	–
$T_e(\text{SIII})(\text{K})$	11,836±354	12,310±149	12,310±149	12,633±298	12,784±813
$N_e(\text{SII})(\text{cm}^{-3})$	55±52	107±14	108±13	111±44	88±73
$\text{O}^+/\text{H}^+(\times 10^5)$	3.054±0.216	2.581±0.128	3.626±1.674	2.790±0.310	3.584±0.766
$\text{O}^{++}/\text{H}^+(\times 10^5)$	9.476±0.629	9.020±0.293	9.020±0.293	8.160±0.469	11.700±1.439
$\text{O}^{+++}/\text{H}^+(\times 10^5)$	–	0.103±0.011	0.112±0.019	–	0.807±0.134
$\text{O}/\text{H}(\times 10^5)$	12.530±0.665	11.700±0.320	12.760±1.700	10.910±0.534	16.090±0.134
12+log(O/H)	8.10±0.02	8.07±0.01	8.11±0.06	8.04±0.02	8.21±0.04
$\text{N}^+/\text{H}^+(\times 10^7)$	9.551±0.551	7.167±0.131	8.332±1.535	6.676±0.251	8.492±0.666
ICF(N)	4.011	4.397	3.480	3.931	1.248
$\text{N}/\text{H}(\times 10^5)$	0.38±0.02	0.32±0.01	0.29±0.05	0.26±0.01	0.38±0.03
12+log(N/H)	6.58±0.03	6.50±0.01	6.46±0.08	6.41±0.02	6.58±0.03
log(N/O)	-1.51±0.03	-1.57±0.01	-1.64±0.10	-1.62±0.03	-1.62±0.06
$\text{Ne}^{++}/\text{H}^+(\times 10^5)$	2.224±0.176	2.876±0.244	2.876±0.244	2.731±0.286	–
ICF(Ne)	1.103	1.097	1.125	1.107	–
$\text{Ne}/\text{H}(\times 10^5)$	2.46±0.19	3.16±0.27	3.24±0.27	3.03±0.32	–
12+log(Ne/H)	7.39±0.03	7.50±0.04	7.51±0.04	7.48±0.05	–
log(Ne/O)	-0.71±0.04	-0.57±0.04	-0.60±0.07	-0.56±0.05	–
$\text{S}^+/\text{H}^+(\times 10^7)$	3.145±0.134	9.900±2.816	9.921±2.823	6.540±1.928	3.702±0.222
$\text{S}^{++}/\text{H}^+(\times 10^7)$	19.790±2.515	19.250±0.900	19.250±0.900	17.190±1.608	20.130±4.913
ICF(S)	1.141	1.164	1.111	1.134	1.337
$\text{S}/\text{H}(\times 10^7)$	26.18±2.87	33.94±3.44	32.42±3.29	26.91±2.85	31.85±6.57
12+log(S/H)	6.42±0.05	6.53±0.04	6.51±0.04	6.43±0.05	6.50±0.09
log(S/O)	-1.68±0.05	-1.54±0.05	-1.59±0.07	-1.61±0.05	-1.70±0.10
$\text{Ar}^{++}/\text{H}^+(\times 10^7)$	–	5.055±0.130	5.055±0.130	4.694±0.280	5.827±0.788
$\text{Ar}^{+++}/\text{H}^+(\times 10^7)$	–	0.557±0.060	0.557±0.060	0.613±0.066	0.000±0.000
ICF(Ar)	–	1.008	1.013	1.010	1.067
$\text{Ar}/\text{H}(\times 10^7)$	–	5.65±0.14	5.69±0.15	5.36±0.29	6.22±0.84
12+log(Ar/H)	–	5.75±0.01	5.75±0.01	5.73±0.02	5.79±0.06
log(Ar/O)	–	-2.32±0.02	-2.35±0.06	-2.31±0.03	-2.41±0.07
$\text{Cl}^{++}/\text{H}^+(\times 10^7)$	0.217±0.055	0.315±0.034	0.315±0.034	0.345±0.041	–
ICF(Cl)	1.356	1.393	1.312	1.345	–
$\text{Cl}/\text{H}(\times 10^7)$	0.29±0.07	0.44±0.05	0.41±0.04	0.47±0.06	–
12+log(Cl/H)	4.47±0.11	4.64±0.05	4.62±0.05	4.67±0.05	–
log(Cl/O)	-3.63±0.11	-3.43±0.05	-3.49±0.07	-3.37±0.06	–
$\text{Fe}^{++}/\text{H}^+(\times 10^7)$	–	1.425±0.122	1.728±0.433	1.590±0.141	–
ICF(Fe)	–	6.006	4.636	5.304	–
log(Fe/O)	–	-2.14±0.04	-2.20±0.12	-2.12±0.04	–
[O/Fe]	–	0.92±0.04	0.98±0.12	0.90±0.04	–

To estimate the possible systematic error associated with different cold zone temperature estimates using the approximated $T_e(\text{OII})$ temperature (Izotov et al. 2006b) for the long-slit spectrum and a direct temperature calculation $T_e(\text{NII})$ based on line ratios $[\text{N II}] \lambda\lambda 5755, 6548, 6584 \text{ \AA}$, column (3) of Table 4 gives calculated abundances using the approximated $T_e(\text{OII})$, and in column (4) the calculated abundances using directly calculated temperature $T_e(\text{NII})$. The specific value of $T_e(\text{OII})$ used in each case is highlighted in bold font in each column. It can

be concluded that although, in general, elemental abundances using the directly computed temperature $T_e(\text{NII})$ are higher, the two values are consistent to within the cited errors. Unfortunately, the intensity of the auroral line $[\text{N II}] \lambda 5755 \text{ \AA}$ is very small (0.15% of the intensity of the line $\text{H}\beta$) and therefore the signal-to-noise ratio for it is only about seven.

The comparison of abundances calculated using the same methodology for two different observational methods and presented in Table 4 (columns (2) and (3)), allows us

to conclude that the calculated abundances agree to within the cited uncertainties. For that reason, the HRS data can be used to study the abundances of chemical elements in bright H II regions and planetary nebulae.

4.2 Comparison with previous results

The measured extinction coefficient, $C(H\beta)$, as well as the extinction value $E(B - V) = 0.68 \cdot C(H\beta)$, in region A2 also agree well for both types of observation with an accuracy of 1.1σ . If we take the foreground extinction of our Galaxy in the IC 4662 direction as $0.19\text{--}0.23$ mag (Schlegel et al. 1998; Schlafly & Finkbeiner 2011), then there is almost no additional extinction in the line-of-sight outside the Milky Way. Here it should be noted that previous work to estimate extinction used either the Balmer line ratio $H\gamma/H\beta$ (Hidalgo-Gómez et al. 2001) or $H\delta$, $H\gamma$ and $H\beta$ (Crowther & Bibby 2009). Where only the $H\delta$, $H\gamma$ and $H\beta$ lines are used to determine the extinction, the total measured value $E(B - V) = 0.36$ mag immediately drops to $E(B - V) = 0.16$ mag, which is in perfect agreement with the measured average extinction value of 0.162 mag for region A2 from Crowther & Bibby (2009).

Our derived abundances of oxygen and neon in the A2 region coincide within the cited uncertainties with previous estimates of abundances of these elements from Heydari-Malayeri et al. (1990); Hidalgo-Gómez et al. (2001); Crowther & Bibby (2009). The nitrogen abundance for the region A2 was obtained earlier in Hidalgo-Gómez et al. (2001) and matches very well with the nitrogen abundance calculated from our data. Gilbert & Vacca (2009) estimated neon and sulphur content using data from Spitzer/IRS infrared spectroscopy. The abundances of these elements are slightly lower than our values, but, unfortunately, there are no errors given in that paper. If we assume that their measured abundances have errors equal to ours (σ_{el} , where subscript 'el' refers to the particular element under discussion), then the difference does not exceed 2 to $3\sigma_{el}$. Also, Gilbert & Vacca (2009) point out a possible systematic shift in their abundances due to the broadening of the measured line, $Hu\alpha$, of the Humphrey series, since the intensities of all lines used by them were related to the intensity of this line.

The abundances of argon, chlorine and iron in the A2 region have been determined for the first time in our work. It is known that α -elements determined from the emission spectra of H II regions are formed in massive stars. As a consequence, it is logical to assume that the abundances of these elements in H II regions are proportional to each other, and for that reason their ratios $\log(Ne/O)$, $\log(S/O)$, $\log(Ar/O)$ and $\log(Cl/O)$ should be constant. For example, the results of Izotov et al. (2006b) based on a very large

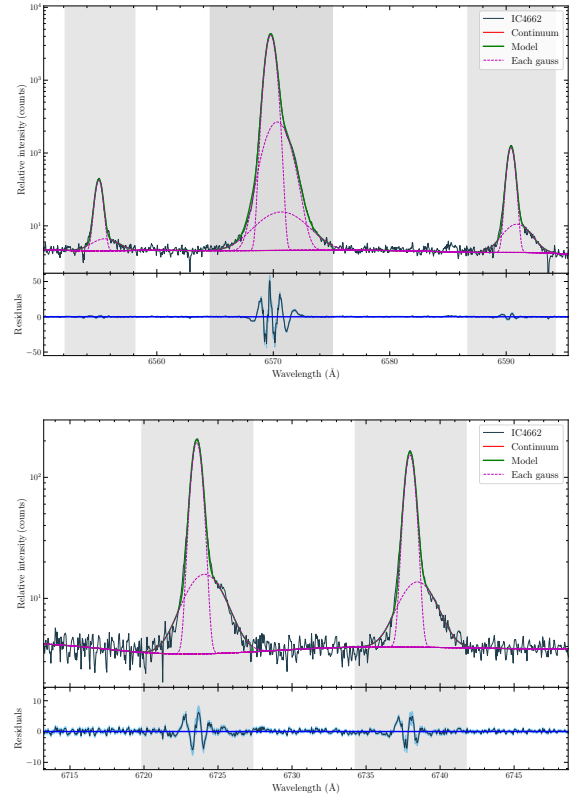


Fig. 6 Components of the different emission lines found in the analysis of the échelle spectrum. The spectral region of the $H\alpha$ line and nitrogen lines $[N\text{ II}] \lambda\lambda 6548, 6583 \text{ \AA}$ is shown in the left plot and the spectral region of the sulphur doublet $[S\text{ II}] \lambda\lambda 6716, 6731 \text{ \AA}$ in the right plot. Both plots consist of two panels. In the upper panels the observed spectrum, the constructed continuum, the emission line components and the full model profile of each line (almost identical to the observed one) are shown on a logarithmic scale. The bottom panels show the difference between the observed spectrum and the model spectrum. The vertical grey bars show the regions for each line within which the approximation by Gaussians was done.

sample of H II galaxies from the DR3 release of the SDSS survey (Abazajian et al. 2005) show that this assumption is correct. As can be seen by comparing the values given in our Table 4 and the dependencies given in Izotov et al. (2006b), all the abundances of α -elements determined by us, as well as their relations to the oxygen abundance, agree very well with these dependencies, which is an additional confirmation of the correctness of the abundances reported here. The iron abundance determined with the weak line $[Fe\text{ III}] \lambda 4658 \text{ \AA}$ is also consistent with the relationship found in Izotov et al. (2006b) and most likely reflects the fact of iron deposition on dust particles.

Table 5 Intensities of the narrow and wide components of emission lines

$\lambda_0(\text{\AA})$ Ion	Narrow component A2				Wide component A2			
	F(λ)/F(H β)	I(λ)/I(H β)	V_{hel} (km s $^{-1}$)	σ_{gas} (km s $^{-1}$)	F(λ)/F(H β)	I(λ)/I(H β)	V_{hel} (km s $^{-1}$)	σ_{gas} (km s $^{-1}$)
3869 [Ne III]	0.5865±0.0492	0.6879±0.0586	299.51	12.42±0.66	0.500±0.243	0.567±0.276	320.86	32.68±3.41
4026 He I	0.0171±0.0023	0.0194±0.0026	300.30	8.49±1.15	—	—	—	—
4069 [S II]	0.0123±0.0019	0.0140±0.0022	300.96	11.60±2.02	—	—	—	—
4102 H δ	0.2770±0.0106	0.3150±0.0126	299.77	10.74±0.15	0.250±0.024	0.274±0.033	325.39	36.04±2.94
4340 H γ	0.4890±0.0167	0.5315±0.0187	299.70	11.42±0.06	0.456±0.028	0.485±0.034	328.40	41.57±1.20
4363 [O III]	0.0699±0.0028	0.0753±0.0030	300.65	10.47±0.16	0.065±0.007	0.069±0.007	320.23	34.11±2.51
4471 He I	0.0452±0.0020	0.0478±0.0021	301.84	10.58±0.28	—	—	—	—
4658 [Fe III]	0.0053±0.0004	0.0055±0.0005	305.59	15.13±0.82	—	—	—	—
4686 He II	—	—	—	—	0.058±0.006	0.059±0.006	321.48	19.23±3.23
4861 H β	1.0000±0.0018	1.0000±0.0024	299.72	10.98±0.02	1.000±0.012	1.000±0.016	325.75	44.59±0.41
4959 [O III]	1.7951±0.0556	1.7667±0.0551	301.10	10.82±0.04	2.084±0.075	2.062±0.075	328.75	37.32±1.22
5007 [O III]	5.4047±0.1653	5.2833±0.1627	301.20	10.79±0.03	6.052±0.206	5.956±0.204	330.50	35.77±1.00
5538 [Cl III]	0.0037±0.0006	0.0034±0.0005	298.27	11.39±2.73	—	—	—	—
5876 He I	0.1307±0.0045	0.1145±0.0041	302.23	11.90±0.10	0.127±0.008	0.115±0.008	330.88	38.50±1.66
6300 [O I]	0.0289±0.0011	0.0241±0.0010	297.13	11.26±0.14	0.036±0.003	0.032±0.003	320.75	46.61±2.60
6312 [S III]	0.0227±0.0009	0.0189±0.0008	298.93	11.84±0.19	0.027±0.003	0.023±0.002	321.54	38.66±5.04
6364 [O I]	0.0112±0.0005	0.0093±0.0005	298.94	13.88±0.25	—	—	—	—
6548 [N II]	0.0254±0.0010	0.0207±0.0008	297.81	10.84±0.09	0.034±0.003	0.029±0.003	317.69	47.31±2.59
6563 H α	3.4681±0.1068	2.8269±0.0951	299.75	10.65±0.01	3.327±0.122	2.844±0.113	327.41	40.38±0.39
6583 [N II]	0.0783±0.0027	0.0637±0.0023	300.88	11.10±0.05	0.100±0.005	0.085±0.005	318.16	45.93±1.19
6678 He I	0.0365±0.0013	0.0294±0.0011	302.47	10.52±0.11	0.042±0.003	0.035±0.003	321.51	40.74±2.61
6716 [S II]	0.1414±0.0005	0.1135±0.0016	301.34	11.56±0.06	0.202±0.004	0.171±0.004	318.15	48.92±0.94
6731 [S II]	0.1083±0.0004	0.0869±0.0013	300.83	11.40±0.07	0.152±0.003	0.129±0.003	317.00	49.01±1.28
7065 He I	0.0349±0.0012	0.0272±0.0011	296.94	11.21±0.06	0.024±0.002	0.020±0.002	329.19	40.32±2.51
7136 [Ar III]	0.1098±0.0036	0.0850±0.0032	299.17	10.23±0.05	0.132±0.006	0.108±0.006	317.33	41.45±1.18
7320 [O II]	0.0398±0.0006	0.0303±0.0007	301.73	12.34±1.40	0.054±0.002	0.044±0.002	319.78	49.45±4.83
7330 [O II]	0.0332±0.0008	0.0253±0.0008	300.51	12.91±1.96	0.045±0.002	0.037±0.002	321.85	48.16±3.15
7751 [Ar III]	0.0283±0.0010	0.0209±0.0009	299.86	9.88±0.07	0.029±0.002	0.023±0.002	322.76	47.25±2.43
8413 P 19	0.0052±0.0004	0.0036±0.0003	301.44	12.68±0.45	—	—	—	—
8438 P 18	0.0056±0.0003	0.0040±0.0003	300.45	11.70±0.25	—	—	—	—
8467 P 17	0.0061±0.0003	0.0043±0.0003	300.81	11.52±0.21	—	—	—	—
8502 P 16	0.0076±0.0004	0.0053±0.0003	300.86	12.45±0.24	—	—	—	—
8545 P 15	0.0090±0.0005	0.0063±0.0004	300.20	12.64±0.33	—	—	—	—
8598 P 14	0.0114±0.0005	0.0079±0.0004	300.54	11.78±0.16	—	—	—	—
8665 P 13	0.0128±0.0006	0.0089±0.0005	302.34	11.58±0.19	—	—	—	—
C(H β) dex	0.27±0.04				0.23±0.05			
EW(H β) Å	98±2				16±1			

Table 6 Intensities of the very wide components

$\lambda_0(\text{\AA})$ Ion	Very Wide Component		
	F(λ)/F(H β)	V_{hel} (km s $^{-1}$)	σ_{gas} (km s $^{-1}$)
4686 He II	44.64±2.38	332.78	393.1±25.1
4959 [O III]	106.01±3.46	349.46	55.8±3.2
5007 [O III]	342.37±8.01	348.26	60.4±1.5
6563 H α	69.27±6.76	344.83	109.5±8.9

4.3 Detected kinematic subsystems in the A2 region

One of the potential features that the high spectral resolution of the échelle data provide is an ability to find and study different kinematic subsystems with different physical conditions (e.g., velocity dispersion of ionised gas and/or abundances of chemical elements) that can be seen in the studied region.

In the case of the A2 region of the IC 4662 galaxy, the échelle data immediately showed the presence of three kinematic subsystems separated in velocity as well as by different velocity dispersions in the ionised gas (hereafter

in the text – simply “gas dispersion”). All lines in the spectrum of region A2 with intensities greater than $\approx 3\%$ of I(H β) allow us with certainty to detect the presence of two components, which in the following text will be referred to as the “narrow component” (NC) and the “broad component” (BC). The measured fluxes of the NC are about 5–7 times larger than those of the BC. An example of such components is shown in Figure 6, where the spectral region of the H α and nitrogen [N II] $\lambda\lambda 6548, 6584$ Å lines is shown in the left plot and of the sulphur doublet [S II] $\lambda\lambda 6716, 6731$ Å in the right plot.

The brightest emission lines, H α and forbidden oxygen lines [O III] $\lambda\lambda 4959, 5007$ Å, also show the presence of a third, “very broad component” (VBC hereafter; see left panel of Figure 6), which is about 5–7 times weaker than the BC. Additionally, the VBC is found in the [He II] $\lambda 4686$ Å line, and this fact will be discussed in Section 5.

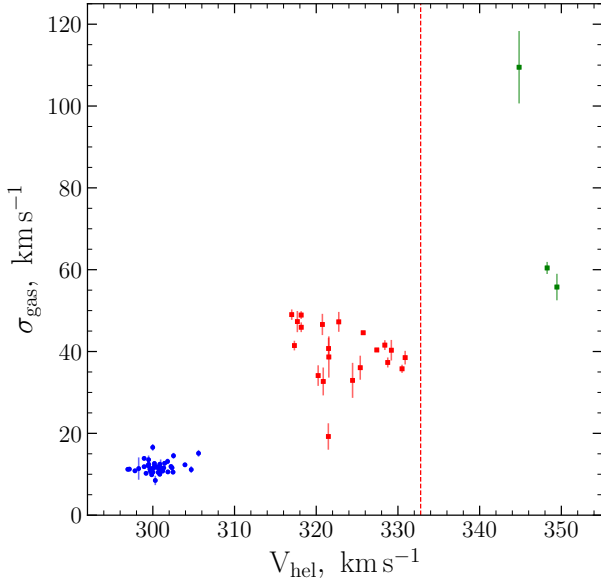


Fig. 7 The distribution of measured heliocentric velocities and gas dispersion for the narrow (blue circles), wide (red squares), and very wide components (green squares) of different emission lines measured during the échelle spectrum analysis. The very wide component of the [He II] $\lambda 4686$ Å line, has a gas dispersion, $\sigma_{gas} = 393$ km s $^{-1}$, and therefore is not shown in the figure, but its velocity is indicated by the red dotted line. 1σ errors are shown with bars, but they are very small in the horizontal direction.

In order to separate these components, each spectral line was fitted with two Gaussians (see Section 3) and no additional constraint on the decomposition was imposed. The result of this decomposition is given in Tables 5 and 6. The decomposition to components is presented only for those lines where the flux error of the BC is less than the measured BC flux itself, otherwise only the NC was considered to be visible. The H α and [O III] $\lambda\lambda 4959, 5007$ Å lines were fitted with three components each. The measured heliocentric velocities for all components of each line and the gas dispersion (σ_{gas}) for these components are shown in Tables 5 and 6 as well. The gas dispersion was recalculated from the measured FWHM of each component using the equation:

$$\sigma_{gas} = 0.43 \sqrt{V_{FWHM}^2 - \Delta V_{therm}^2 - \Delta V_{instr}^2} \quad (4)$$

where ΔV_{instr} is the velocity correction recalculated from the instrumental FWHM correction (equations 1 and 2 from this paper), and ΔV_{therm} is the correction for temperature broadening, which was calculated as in Lang (1980):

$$\Delta V_{therm} = 21.4 \sqrt{\frac{T_e(\text{ion})}{10^4 \cdot A(\text{ion})}} \quad (5)$$

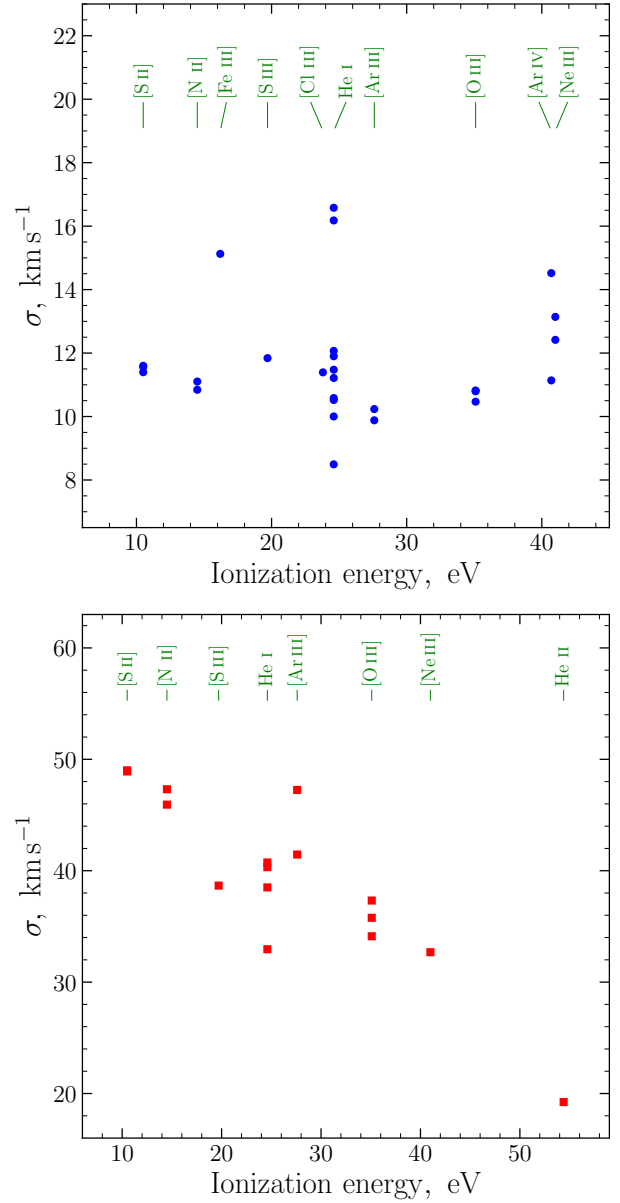


Fig. 8 The measured gas dispersion for different emission lines as a function of the consecutive ionization energy of atoms of different elements. The left panel shows this dependence for the NC, and the right panel for the BC.

where $T_e(\text{ion})$ is the electron temperature of the corresponding ion from Table 4, and $A(\text{ion})$ is the atomic weight of that ion. Since the measurements of the emission line centre have a very small formal error (only some meters per second), they are not given in Table 5, and the characteristic accuracy of radial velocity determination is taken to be the accuracy of the dispersion curve for LR échelle spectra, 300–400 m s $^{-1}$.

Figure 7 shows the distribution of heliocentric velocities versus gas dispersion for the NC (blue circles), BC (red squares) and VBC (green squares) for different spec-

tral lines. We see that the distribution of heliocentric velocities and gas dispersions shows the presence of two, well separated, kinematic subsystems: the NC subsystem and the BC subsystem. The mean heliocentric velocity of the NC subsystem is $V_{\text{hel}} = 300.05 \pm 2.08 \text{ km s}^{-1}$, and for the BC subsystem is $V_{\text{hel}} = 323.25 \pm 4.47 \text{ km s}^{-1}$. The mean gas dispersion of the NC subsystem is $\sigma_{\text{gas}} = 11.90 \pm 2.44 \text{ km s}^{-1}$, and for the BC subsystem is $\sigma_{\text{gas}} = 39.97 \pm 6.85 \text{ km s}^{-1}$. It can be assumed that the real accuracy of the mean heliocentric velocity is better than the above, and an additional scatter is due to the fact that lines of different elements have slightly different heliocentric velocities. For example, the mean heliocentric velocity of the NC subsystem measured with lines of the Balmer and Paschen series only is $V_{\text{hel}} = 300.38 \pm 0.80 \text{ km s}^{-1}$ with a mean gas dispersion $\sigma_{\text{gas}} = 11.60 \pm 0.71 \text{ km s}^{-1}$. A similar picture can be seen for the VBC, where both gas dispersions and heliocentric velocities are slightly different for hydrogen and oxygen but they are very close for both oxygen lines.

Figure 8 shows the dependence of the measured gas dispersion for different emission lines as a function of the consecutive ionisation energy of atoms of these elements. The left panel shows this dependence for the NC of emission lines, and the right panel for the BC of emission lines. The idea behind this picture is that in the case of a central ionising source that is losing (has lost) some of its mass in the form of a stellar wind or of dropped shells, and because of the stratification of the ionised gas region around this source (as in the case of planetary nebulae), the outer, colder regions of the nebula (H II region) expand with higher velocities (e.g., Medina et al. 2006; Richer et al. 2008; Jacob et al. 2013).

The measured fluxes of the emission line components presented in Table 5, were used to calculate abundances of chemical elements, which are shown in columns (5) and (6) of Table 4. For uniformity, the cold zone temperature was calculated using the approximated temperature $T_e(\text{OII})$ in both cases. The comparison shows that the calculated abundances of oxygen and nitrogen for the BC are higher than the abundances calculated for the NC and this difference is about $3.3\sigma_{el}$ in oxygen and $4.3\sigma_{el}$ in nitrogen. For sulphur and argon the calculated abundances for the BC are higher than those for the NC as well but these differences are less than $1\sigma_{el}$ due to very large errors.

5 DISCUSSION

An échelle spectrum of the H II region A2 in the irregular galaxy IC 4662 shows the presence of three spectral components (NC, BC and VBC), which differ in: (1) the mean velocity dispersion, (2) the average heliocentric velocity, (3) the integral flux of components in each line, (4) the

abundance of chemical elements (for NC and BC only), and (5) the behaviour of the measured gas dispersion for the different emission lines as a function of the sequential ionization energy (for NC and BC only).

Additionally, (1) it can be argued that both the BC and the VBC of the [He II] $\lambda 4686 \text{ \AA}$ line in terms of velocities belong to the region of the BC, since the difference in velocity for the NC [He II] $\lambda 4686 \text{ \AA}$ line (332.78 km s^{-1}) and the average BC velocity (323.25 km s^{-1}) is only $2.1\sigma_{el}$; (2) the strong line ratios used in the BPT diagrams (Baldwin et al. 1981) for both components (NC: $\log([\text{O III}] \lambda 5007/H\beta) = 0.72 \pm 0.01$, $\log([\text{N II}] \lambda 6584/H\alpha) = -1.65 \pm 0.02$; WC: $\log([\text{O III}] \lambda 5007/H\beta) = 0.78 \pm 0.03$, $\log([\text{N II}] \lambda 6584/H\alpha) = -1.52 \pm 0.03$) show that we are practically dealing with pure photoionization excitation.

Altogether, it can be assumed that the region generating the NC in the échelle spectrum is the main body of the H II region A2, whose gas is well mixed, and the recorded gas dispersion mainly characterizes the turbulent velocity of this gas since its σ_{gas} looks practically constant in the left panel of Figure 8. A detailed study of H I in IC 4662 (van Eymeren et al. 2010) found the systemic velocity of the galaxy to be $V_{sys}(\text{H I}) = 302 \text{ km s}^{-1}$, which agrees very well with the mean velocity of the NC region found from our data. The oxygen abundance we calculated for the NC (see Table 4) also agrees very well with the oxygen abundance for the same region from Crowther & Bibby (2009) (region #3 with $\text{O/H} = 8.06 \pm 0.03 \text{ dex}$).

The BC is apparently formed in a separate region around young, hot stars (or just a single hot massive star), the wind from which “injects” mechanical energy into the surrounding space and encourages the expansion of the jet-tionised matter enriched with chemical elements. This hot massive star (stars) is a central ionising source for this region as well. For the BC region, the contribution of turbulent gas velocity is probably smaller than that of expansion and the expansion velocity is close to the σ_{gas} of the outermost region, $\sim 50 \text{ km s}^{-1}$ (bottom panel of Figure 8).

The presence of the VBC of the He II $\lambda 4686 \text{ \AA}$ line indicates that this region is most likely associated with the presence of a Wolf-Rayet star (WR hereafter). Crowther & Bibby (2009) studied the H II regions A1 and A2 of the IC 4662 galaxy using images from different filters on the Hubble Space Telescope and the VLT telescope. In their study, they found six WR stars in these two H II regions and showed their positions. Comparison of the position of the échelle object fibre during the SALT observations (see bottom panel of Figure 1 of this paper) and the positions of WR stars detected by Crowther & Bibby (2009) (see Figure 2 of that work) shows that the HRS fibre was placed on that part of the A2 region which contains WR

star A2–WR2. The spectral aperture #3 of Crowther & Bibby (2009) included two WR stars, A2–WR2 and A2–WR3, and these authors suggested that one of those stars could be a WC star and the other a WN5–6 star. Our spectral échelle data do not show any additional lines of the WR star other than the He II $\lambda 4686$ Å line. However, it should be noted here that the level of accumulated signal in the spectral region ~ 5800 Å is much higher than in the blue 4600–4700 Å region because of the overall sensitivity of the spectrograph. Since there is no indication of the presence of a broad C IV $\lambda 5801 - 12$ line in the échelle spectrum, the absence of these spectral lines unequivocally confirms that the star A2–WR2 is of the WN type rather than the WC type. The measured FWHM = 14.31 Å for the emission line allows refinement of its ionization subclass to WN7–8 (Smith et al. 1996). The expected accuracy of such classification is approximately ± 1 subclass with a probability of $\sim 80\%$ (Hamann et al. 2006). Additional confirmation of its classification as a late WN (WNL) star comes from the enhanced nitrogen content in the emission spectrum, which is characteristic of regions enriched by the ejecta of WNL stars.

Most of the WR stars found in Crowther & Bibby (2009) are located on the edges of the H II regions, A1 and A2. It is known that most of the studied WR stars in our Galaxy are also located outside known stellar clusters. And since most massive stars are born in clusters (e.g. Zinnecker & Yorke 2007) it is assumed that most of the WR stars studied have been ejected from parent clusters. Such stars could be ejected either by dynamic processes in the cluster core (Poveda et al. 1967; Gies & Bolton 1986) or as a result of a supernova explosion in a close system of two massive stars (Blaauw 1961; Stone 1991). In both scenarios, the ejected WR star must be located close to the parent cluster, since the precursor WR star is a very massive star with a mass of at least $25 M_{\odot}$, having a lifetime of at most 5 Myr. Detailed studies of individual WR stars in our Galaxy find their inferred mother clusters based on the observed radial velocities of these stars and their proper motions (e.g. Gvaramadze et al. 2009, 2010b; Burgemeister et al. 2013). Therefore, the velocity of the NC from our study can naturally be interpreted as the velocity of the parent H II region A2, which closely matches the systemic velocity of the galaxy. In this framework, the velocity of the BC is interpreted as the velocity of the circumstellar envelope surrounding the WN star (as well as the velocity of star itself). The velocity difference, $dV = (V_{hel}^{BC} - V_{hel}^{NC}) = 23$ km/s, represents the radial component of the ejection velocity from the parent cluster located within H II region A2. This interpretation is further supported by the location of the WN star at the edge of H II region A2 (see the right panel of Figure 1).

Modern studies of the evolution of WR stars and their circumstellar envelopes distinguish two types of envelope. In the first case, these are compact envelopes of very young WR stars of WNL type, where the stellar wind is still confined to the region occupied by circumstellar matter dumped at a previous stage of red supergiant (RSG) or LBV evolution and therefore show the signatures of CNO-processing (e.g. Chu 1981; Lozinskaya & Tutukov 1981; Gruendl et al. 2000; Gvaramadze et al. 2010a). On the other hand, winds from more evolved WR stars of WNE type interact directly with the local interstellar medium and create more extended envelopes, whose abundances of chemical elements are equal to the abundances of the surrounding H II regions (e.g., Esteban et al. 1992; Stock et al. 2011). Our analysis shows that the abundance of the chemical elements, oxygen and nitrogen, in the BC region is systematically higher than the abundance of the same elements in the NC region, which is the main body of the A2 region. This result also fits logically into the picture of ejected stellar material around a very young WN star where a fast wind has caught up with material enriched with fusion products previously shed by the RSG, and contributes to its expansion. Since its ionisation subclass is WN7–8 it is quite possible that the fast WR wind is still just passing through the zone created by the slow RSG wind (Gvaramadze et al. 2009).

Let us now support the proposed ideas with various estimates based on existing models:

(1) According to the models of Weaver et al. (1977) and Chevalier & Clegg (1985), the expansion velocity of a shell created by the wind of a massive star can be estimated as $v_{exp} \propto (L_w/n)^{(1/5)}$, where L_w is the mechanical luminosity of the wind, and n is the density of the surrounding medium. The mechanical luminosity of the wind can be calculated using the formula $L_w = (1/2)\dot{M}v_{\infty}^2$, where \dot{M} is the mass-loss rate, and v_{∞} is the terminal wind velocity. For WR stars of type WN7-8, these parameters can be taken from Table 1 of Crowther (2007) as $\dot{M} = 5 \times 10^{-5} M_{\odot}/year$, $v_{\infty} = 1000$ km s $^{-1}$, leading to an estimated mechanical wind luminosity of $L_w \approx 10^{36} - 10^{37}$ erg/s. Using the measured electron density $n_e \approx 100$ cm $^{-3}$, the theoretical expansion velocity is expected to be $\sim 30 - 60$ km s $^{-1}$, which is in good agreement with the measured velocity dispersion of the SC ≈ 40 km s $^{-1}$.

(2) Since the size of the studied giant H II region is approximately 25 pc, using the average expansion velocity, the age of the shell can be estimated as $t_{age} \approx R_{shell}/v_{exp} \approx 12.5/40 \approx 3 \times 10^5$ years, which is consistent with the short evolutionary phase of WR stars following the red supergiant (RSG) stage.

(3) For a WN7-8 star, the typical terminal wind velocity is

$v_\infty \approx 1000 - 1200 \text{ km s}^{-1}$ (Hamann et al. 2006; Crowther 2007). Then, the ratio $\sigma(\text{He II } \lambda 4686)/v_\infty \approx 0.3$, which is consistent with theoretical models of line formation in WR star winds (Hillier 1991).

(4) Nitrogen enrichment (a difference with a significance of 4.4σ between NC and BC) quantitatively supports the assumption that the material was ejected during the previous RSG/LBV stage. The typical increase in nitrogen content in shells following the RSG phase is 0.2–0.4 dex (Lamers et al. 2001), which corresponds to the observed difference of 0.22 dex between NC and BC.

5.1 Very Broad Component

The VBC is observed in many irregular galaxies (for example, Oparin et al. 2020; Bresolin et al. 2020; Egorov et al. 2021) and is associated with the action of winds from massive stars. This component represents a unique “window” into the processes occurring in the immediate vicinity of the WR star. The extreme velocity dispersion of the VBC in the He II $\lambda 4686 \text{ \AA}$ line is directly linked to the fast wind of the WR star and corresponds to approximately 1/3 of the expected terminal wind velocity for a WN7–8 type star (see above). Significantly lower, but still high dispersions of the VBC in the [O III] $\lambda 5007 \text{ \AA}$ and $\text{H}\alpha$ lines (see Table 6) indicate the presence of stratification in the wind acceleration region.

The three-component structure (VBC, BC, NC) is, in essence, a direct observation of different zones in the classical wind bubble model (Weaver et al. 1977): the VBC in the He II line corresponds to the freely flowing wind zone, the VBC in the [O III] $\lambda 5007 \text{ \AA}$ and $\text{H}\alpha$ lines corresponds to the hot gas behind the shock front, whilst the BC corresponds to the compressed shell of cooled gas at the boundary with the surrounding interstellar medium. The relatively low intensity of the VBC (approximately 5–7 times weaker than the BC) is consistent with the small filling factor of hot gas in such a structure. The difference in radial velocities between the VBC components (Table 6) may indicate non-spherical expansion or the presence of asymmetry in the density distribution of the surrounding medium, which is consistent with modern 3D models of the interaction of WR star winds with a heterogeneous medium (van Marle et al. 2011).

It should be noted that the observation of the VBC with such characteristics in a low-metallicity environment provides valuable information about the influence of heavy element content on stellar wind properties and their interaction with the surrounding medium. In systems with low metallicity, a decrease in both the mass loss rate and terminal wind velocity of WR stars is expected (Vink & de Koter 2005). The presented observations show that even

under such conditions, stellar wind is capable of creating a complex dynamic structure in the surrounding environment, which has important implications for understanding the feedback of massive stars in the early Universe.

5.2 Implications for galaxy evolution

In general, observations of the H II region A2 in the IC 4662 galaxy provide important information about star formation processes and feedback in low-metallicity environments:

(1) The detection of significant differences in chemical composition (0.15–0.20 dex) between kinematic subsystems on a scale of only 25 pc confirms that local enrichment plays a substantial role in the chemical evolution of dwarf galaxies, contrary to the widespread belief about rapid and complete mixing of the interstellar medium in these systems. In Kniazev et al. (2005), the authors indicated that despite the established conviction that the interstellar medium in irregular galaxies is well mixed, very often information about the average metallicity of such galaxies is known with an accuracy of up to 0.3–0.4 dex, which is related both to possible processes of local enrichment and an insufficient number of quality observations.

(2) The identification of an expanding shell around the WR star with increased nitrogen content demonstrates “in action” the mechanism of interstellar medium enrichment with products of massive star evolution. This is especially important for understanding the early stages of the chemical evolution of the Universe, when similar processes could dominate in primordial galaxies.

(3) The effective mechanical impact of the WR star wind on the surrounding environment even in low-metallicity conditions indicates that stellar feedback may be a key factor in regulating star formation in metal-poor systems. The expanding shell not only distributes enriched material, but also may create conditions for the triggered formation of the next generation of stars.

(4) The discovery of the complex kinematic structure of the H II region A2 with three different components emphasises the need to develop multiphase models of the interstellar medium in low-metallicity galaxies for adequate interpretation of observations and understanding of feedback cycles between star formation and interstellar medium properties.

6 CONCLUSIONS

The bright H II region A2 of the irregular galaxy IC 4662 was studied using long-slit and échelle spectroscopy at the SALT telescope. This work has shown that:

1. The calculated abundances of chemical elements obtained from different spectral data are consistent with

each other within the available errors, and hence the spectral data obtained from the HRS échelle spectrograph, corrected for the spectral sensitivity curve, can be used to determine the abundances of chemical elements of emission nebulae.

2. The analysis of échelle data revealed three spectral components, apparently belonging to different subsystems of the investigated H II region. Their physical and kinematic characteristics were compared, as were the abundances of the chemical elements, oxygen, nitrogen, sulphur and argon, which were calculated using the T_e method.

3. The analysis of échelle data as well as a comparison with previous studies of the region A2 in IC 4662 allowed us to suggest that one of the detected subsystems belongs to the region around a hot young WR star of WNL type, which has been ejected from the parent cluster located in the main body of region A2. The wind from this WR star “injects” mechanical energy into the surrounding area and contributes to the expansion of the envelope shed in a previous stage of evolution (red supergiant or LBV) and enriched with chemical elements. This assumption is very well supported by comparisons with theoretical models.

Acknowledgements This work is based on observations obtained with the Southern African Large Telescope (SALT), program 2017-1-MLT-001 (PI: Kniazev). A.Y. acknowledges support from the National Research Foundation (NRF) of South Africa. The author expresses gratitude to the anonymous reviewer for comments and suggestions, which helped to improve the description of the obtained results and their interpretation.

References

- Abazajian, K., Adelman-McCarthy, J. K., Agüeros, M. A., et al. 2005, *AJ*, 129, 1755 [10](#)
- Baldwin, J. A., Phillips, M. M., & Terlevich, R. 1981, *PASP*, 93, 5 [13](#)
- Barnes, S. I., Cottrell, P. L., Albrow, M. D., et al. 2008, *Society of Photo-Optical Instrumentation Engineers (SPIE) Conference Series*, Vol. 7014, The optical design of the Southern African Large Telescope high resolution spectrograph: SALT HRS, *Society of Photo-Optical Instrumentation Engineers (SPIE) Conference Series*, Vol. 7014, Ground-based and Airborne Instrumentation for Astronomy II. Edited by McLean, Ian S.; Casali, Mark M. *Proceedings of the SPIE*, Volume 7014, article id. 70140K, 12 pp. (2008), 70140K [3](#)
- Blaauw, A. 1961, *BAN*, 15, 265 [14](#)
- Bramall, D. G., Sharples, R., Tyas, L., et al. 2010, *Society of Photo-Optical Instrumentation Engineers (SPIE) Conference Series*, Vol. 7735, The SALT HRS spectrograph: final design, instrument capabilities, and operational modes, *Society of Photo-Optical Instrumentation Engineers (SPIE) Conference Series*, Vol. 7735, *Proceedings of the SPIE*, Volume 7735, id. 77354F (2010), 77354F [3](#)
- Bramall, D. G., Schmoll, J., Tyas, L. M. G., et al. 2012, *Society of Photo-Optical Instrumentation Engineers (SPIE) Conference Series*, Vol. 8446, The SALT HRS spectrograph: instrument integration and laboratory test results, *Society of Photo-Optical Instrumentation Engineers (SPIE) Conference Series*, Vol. 8446, Ground-based and Airborne Instrumentation for Astronomy IV. *Proceedings of the SPIE*, Volume 8446, article id. 84460A, 9 pp. (2012), 84460A [3](#)
- Bresolin, F., Rizzi, L., Ho, I. T., et al. 2020, *MNRAS*, 495, 4347 [15](#)
- Buckley, D. A. H., Swart, G. P., & Meiring, J. G. 2006, *Society of Photo-Optical Instrumentation Engineers (SPIE) Conference Series*, Vol. 6267, Completion and commissioning of the Southern African Large Telescope, *Society of Photo-Optical Instrumentation Engineers (SPIE) Conference Series*, Vol. 6267, Ground-based and Airborne Telescopes. Edited by Stepp, Larry M. *Proceedings of the SPIE*, Volume 6267, id. 62670Z (2006), 62670Z [1](#)
- Burgemeister, S., Gvaramadze, V. V., Stringfellow, G. S., et al. 2013, *MNRAS*, 429, 3305 [14](#)
- Burgh, E. B., Nordsieck, K. H., Kobulnicky, H. A., et al. 2003, *Society of Photo-Optical Instrumentation Engineers (SPIE) Conference Series*, Vol. 4841, Prime Focus Imaging Spectrograph for the Southern African Large Telescope: optical design, ed. M. Iye & A. F. M. Moorwood, *Society of Photo-Optical Instrumentation Engineers (SPIE) Conference Series*, Vol. 4841, Instrument Design and Performance for Optical/Infrared Ground-based Telescopes. Edited by Iye, Masanori; Moorwood, Alan F. M. *Proceedings of the SPIE*, Volume 4841, pp. 1463-1471 (2003), ed. M. Iye & A. F. M. Moorwood, 1463 [2](#)
- Chevalier, R. A., & Clegg, A. W. 1985, *Nature*, 317, 44 [14](#)
- Chu, Y. H. 1981, *ApJ*, 249, 195 [14](#)
- Crause, L. A., Sharples, R. M., Bramall, D. G., et al. 2014, *Society of Photo-Optical Instrumentation Engineers (SPIE) Conference Series*, Vol. 9147, Performance of the Southern African Large Telescope (SALT) High Resolution Spectrograph (HRS), *Society of Photo-Optical Instrumentation Engineers (SPIE) Conference Series*, Vol. 9147, *Proceedings of the SPIE*, Volume 9147, id. 91476T 14 pp. (2014), 91476T [3](#)
- Crawford, S. M., Still, M., Schellart, P., et al. 2010, *Society of Photo-Optical Instrumentation Engineers (SPIE) Conference Series*, Vol. 7737, PySALT: the

- SALT science pipeline, Society of Photo-Optical Instrumentation Engineers (SPIE) Conference Series, Vol. 7737, Proceedings of the SPIE, Volume 7737, id. 773725 (2010)., 773725 [3](#), [4](#)
- Crowther, P. A. 2007, *ARA&A*, 45, 177 [14](#), [15](#)
- Crowther, P. A., & Bibby, J. L. 2009, *A&A*, 499, 455 [2](#), [10](#), [13](#), [14](#)
- Egorov, O. V., Lozinskaya, T. A., Vasiliev, K. I., et al. 2021, *MNRAS*, 508, 2650 [15](#)
- Esteban, C., Vilchez, J. M., Smith, L. J., & Clegg, R. E. S. 1992, *A&A*, 259, 629 [14](#)
- Gies, D. R., & Bolton, C. T. 1986, *ApJS*, 61, 419 [14](#)
- Gilbert, A. M., & Vacca, W. D. 2009, *Astrophysics and Space Science*, 324, 147 [2](#), [10](#)
- Gruendl, R. A., Chu, Y.-H., Dunne, B. C., & Points, S. D. 2000, *AJ*, 120, 2670 [14](#)
- Gvaramadze, V. V., Kniazev, A. Y., Fabrika, S., et al. 2010a, *MNRAS*, 405, 520 [14](#)
- Gvaramadze, V. V., Kniazev, A. Y., Hamann, W. R., et al. 2010b, *MNRAS*, 403, 760 [14](#)
- Gvaramadze, V. V., Fabrika, S., Hamann, W. R., et al. 2009, *MNRAS*, 400, 524 [14](#)
- Hamann, W. R., Gräfener, G., & Liermann, A. 2006, *A&A*, 457, 1015 [14](#), [15](#)
- Hamuy, M., Suntzeff, N. B., Heathcote, S. R., et al. 1994, *PASP*, 106, 566 [3](#)
- Hamuy, M., Walker, A. R., Suntzeff, N. B., et al. 1992, *PASP*, 104, 533 [3](#)
- Heydari-Malayeri, M., Melnick, J., & Martin, J. M. 1990, *A&A*, 234, 99 [2](#), [10](#)
- Hidalgo-Gómez, A. M., Masegosa, J., & Olofsson, K. 2001, *A&A*, 369, 797 [2](#), [10](#)
- Hillier, D. J. 1991, *A&A*, 247, 455 [15](#)
- Izotov, Y. I., Schaerer, D., Blecha, A., et al. 2006a, *A&A*, 459, 71 [1](#)
- Izotov, Y. I., Stasińska, G., Meynet, G., Guseva, N. G., & Thuan, T. X. 2006b, *A&A*, 448, 955 [6](#), [9](#), [10](#)
- Jacob, R., Schönberner, D., & Steffen, M. 2013, *A&A*, 558, A78 [13](#)
- James, B. L., Tsamis, Y. G., Barlow, M. J., Walsh, J. R., & Westmoquette, M. S. 2013a, *MNRAS*, 428, 86 [1](#)
- James, B. L., Tsamis, Y. G., Barlow, M. J., et al. 2009, *MNRAS*, 398, 2 [1](#)
- James, B. L., Tsamis, Y. G., Walsh, J. R., Barlow, M. J., & Westmoquette, M. S. 2013b, *MNRAS*, 430, 2097 [1](#)
- Johnson, K. E., Indebetouw, R., & Pisano, D. J. 2003, *AJ*, 126, 101 [2](#)
- Kaisin, S. S., Kasparova, A. V., Kniazev, A. Y., & Karachentsev, I. D. 2007, *Astronomy Letters*, 33, 283 [2](#)
- Kniazev, A. Y. 2012, *Astronomy Letters*, 38, 707 [6](#)
- Kniazev, A. Y. 2021, *Astrophysical Bulletin* (in press), 11 [3](#)
- Kniazev, A. Y., Grebel, E. K., Pustilnik, S. A., Pramskij, A. G., & Zucker, D. B. 2005, *AJ*, 130, 1558 [6](#), [15](#)
- Kniazev, A. Y., Gvaramadze, V. V., & Berdnikov, L. N. 2016, *MNRAS*, 459, 3068 [4](#)
- Kniazev, A. Y., Pustilnik, S. A., Grebel, E. K., Lee, H., & Pramskij, A. G. 2004, *ApJS*, 153, 429 [5](#), [6](#)
- Kniazev, A. Y., Usenko, I. A., Kovtyukh, V. V., & Berdnikov, L. N. 2019, *Astrophysical Bulletin*, 74, 208 [4](#)
- Kniazev, A. Y., Zijlstra, A. A., Grebel, E. K., et al. 2008, *MNRAS*, 388, 1667 [6](#), [8](#)
- Kobulnicky, H. A., Nordsieck, K. H., Burgh, E. B., et al. 2003, Society of Photo-Optical Instrumentation Engineers (SPIE) Conference Series, Vol. 4841, Prime focus imaging spectrograph for the Southern African large telescope: operational modes, ed. M. Iye & A. F. M. Moorwood, Society of Photo-Optical Instrumentation Engineers (SPIE) Conference Series, Vol. 4841, Instrument Design and Performance for Optical/Infrared Ground-based Telescopes. Edited by Iye, Masanori; Moorwood, Alan F. M. Proceedings of the SPIE, Volume 4841, pp. 1634-1644 (2003)., ed. M. Iye & A. F. M. Moorwood, 1634 [2](#)
- Lamers, H. J. G. L. M., Nota, A., Panagia, N., Smith, L. J., & Langer, N. 2001, *ApJ*, 551, 764 [15](#)
- Lang, K. R. 1980, *Astrophysical Formulae. A Compendium for the Physicist and Astrophysicist*. [12](#)
- Lozinskaya, T. A., & Tutukov, A. V. 1981, *Nauchnye Informatsii*, 49, 21 [14](#)
- McQuinn, K. B. W., Skillman, E. D., Cannon, J. M., et al. 2009, *ApJ*, 695, 561 [2](#)
- McQuinn, K. B. W., Skillman, E. D., Cannon, J. M., et al. 2010a, *ApJ*, 721, 297 [2](#)
- McQuinn, K. B. W., Skillman, E. D., Cannon, J. M., et al. 2010b, *ApJ*, 724, 49 [2](#)
- Medina, S., Peña, M., Morisset, C., & Stasińska, G. 2006, *Revista Mexicana de Astronomía y Astrofísica*, 42, 53 [13](#)
- O'Donoghue, D., Buckley, D. A. H., Balona, L. A., et al. 2006, *MNRAS*, 372, 151 [1](#)
- Oparin, D. V., Egorov, O. V., & Moiseev, A. V. 2020, *Astrophysical Bulletin*, 75, 361 [15](#)
- Poveda, A., Ruiz, J., & Allen, C. 1967, *Boletín de los Observatorios Tonantzintla y Tacubaya*, 4, 86 [14](#)
- Richer, M. G., López, J. A., Pereyra, M., et al. 2008, *ApJ*, 689, 203 [13](#)
- Schlafly, E. F., & Finkbeiner, D. P. 2011, *ApJ*, 737, 103 [10](#)
- Schlegel, D. J., Finkbeiner, D. P., & Davis, M. 1998, *ApJ*, 500, 525 [10](#)
- Smith, L. F., Shara, M. M., & Moffat, A. F. J. 1996,

- MNRAS, 281, 163 [14](#)
- Stock, D. J., Barlow, M. J., & Wesson, R. 2011, MNRAS, 418, 2532 [14](#)
- Stone, R. C. 1991, AJ, 102, 333 [14](#)
- van Eymeren, J., Koribalski, B. S., López-Sánchez, Á. R., Dettmar, R.-J., & Bomans, D. J. 2010, MNRAS, 407, 113 [2](#), [13](#)
- van Marle, A. J., Meliani, Z., Keppens, R., & Decin, L. 2011, ApJL, 734, L26 [15](#)
- Vink, J. S., & de Koter, A. 2005, A&A, 442, 587 [15](#)
- Weaver, R., McCray, R., Castor, J., Shapiro, P., & Moore, R. 1977, ApJ, 218, 377 [14](#), [15](#)
- Zinnecker, H., & Yorke, H. W. 2007, ARA&A, 45, 481 [14](#)